International Journal of Hydrogen Energy 92 (2024) 1448–1462

Contents lists available at ScienceDirect

International Journal of Hydrogen Energy

journal homepage: www.elsevier.com/locate/he

Exploiting the Ocean Thermal Energy Conversion (OTEC) technology for green hydrogen production and storage: Exergo-economic analysis

Lorenzo Ciappi [a], Luca Socci [b], Mattia Calabrese [b], Chiara Di Francesco [b], Federica Savelli [b], Giampaolo Manfrida [b], Andrea Rocchetti [b], Lorenzo Talluri [b], Daniele Fiaschi [b,*]

[a] University of Birmingham, School of Chemical Engineering, Birmingham, United Kingdom
[b] University of Florence, Department of Industrial Engineering, Firenze, Italy

ARTICLE INFO

Handling Editor: Dr F Gallucci

Keywords:
Ocean thermal energy conversion (OTEC)
Hydrogen
Exergy
Exergo-economic
Electrolysis
Renewable energy

ABSTRACT

This study presents and analyses three plant configurations of the Ocean Thermal Energy Conversion (OTEC) technology. All the solutions are based on using the OTEC system to obtain hydrogen through an electrolyzer. The hydrogen is then compressed and stored. In the first and second layouts, a Rankine cycle with ammonia and a mixture of water and ethanol is utilised respectively; in the third layout, a Kalina cycle is considered. In each configuration, the OTEC cycle is coupled with a polymer electrolyte membrane (PEM) electrolyzer and the compression and storage system. The water entering the electrolyzer is pre-heated to 80 °C by a solar collector. Energy, exergy, and exergo-economic studies were conducted to evaluate the cost of producing, compressing, and storing hydrogen. A parametric analysis examining the main design constraints was performed based on the temperature range of the condenser, the mass flow ratio of hot and cold resource flows, and the mass fraction. The maximum value of the overall exergy efficiency calculated is equal to 93.5% for the Kalina cycle, and 0.524 €/kWh is the minimum cost of hydrogen production achieved. The results were compared with typical data from other hydrogen production systems.

1. Introduction

The substantial increase in energy demand, together with the progressive reduction of fossil resources and the rise of pollutant and greenhouse emissions, have led to a global effort to foster the exploitation of renewable resources. In this scenario, the sea has enormous potential due to its extension and the power conveyed. In particular, the thermal gradients of the sea may be harnessed for energy provision, and the worldwide availability of ocean thermal energy is estimated at about $4.4 \bullet 10^{16}$ kWh per year [1]. Ocean Thermal Energy Conversion (OTEC) is a technology that transforms seawater heat into mechanical energy for obtaining electric energy. These systems implement thermodynamic cycles exploiting the temperature difference between shallow and deep ocean waters, which is primarily disposable in tropical and subtropical areas. In these locations, the variation in temperature for the warm and the cold seawater ranges from 22 °C to 26 °C. Indeed, the surface water temperature is about 28–30 °C, and the deep water temperature is around 4–6 °C at about 1000 m underwater [2]. The proper selection of the application site is paramount for realizing a sustainable project. The efficiency of energy conversion depends mainly on the sea depth, the magnitude of the temperature difference between the surface seawater and the deep seawater, and its variations over time [3,4]. It was assessed that almost 100 countries fulfil the strict oceanographic and climatic criteria for installing these facilities [5]. The OTEC systems can use an open cycle or a closed cycle. The former layout uses seawater as the working fluid. It is pumped inside the low-pressure chamber, where it is evaporated due to the temperature and pressure conditions. The vapour expands and drives a steam turbine connected to an electric generator. Afterwards, the vapour is condensed through refrigeration with cold water. Either warm or cold streams of water are discharged back into the sea. Conversely, the latter layout utilises a liquid with a low boiling point as the working fluid. This liquid is evaporated by heat transfer with the warm seawater, and its vapour moves the steam turbine. Then, it is condensed by the cold water of the deep sea and pumped to the evaporator for the cyclical functioning of the system. The main advantage of a closed cycle is the reduction of the dimensions of the system components regarding an open cycle, which is achievable through the selection of the working fluid. Moreover, the maintenance costs are

* Corresponding author.
E-mail address: daniele.fiaschi@unifi.it (D. Fiaschi).

https://doi.org/10.1016/j.ijhydene.2024.10.290
Received 20 April 2024; Received in revised form 17 October 2024; Accepted 20 October 2024
Available online 3 November 2024

lower for the closed-cycle systems as they do not need to guarantee the absence of leakage in the pressurized chamber for water evaporation. On the contrary, they require large heat exchangers made of expensive materials to reliably operate in a chemically aggressive environment like the sea [6]. In addition, stringent safety requirements need to be implemented to prevent the emission of their working fluid into the atmosphere. It is worth noting even that closed-cycle systems do not allow to obtain the freshwater condensed by the open-cycle systems during their operation. A recent economic analysis indicates that ocean thermal energy conversion can be competitive in four markets in the next few years [7]. The first one is the small island of Molokai in Hawaii, where a small open-cycle OTEC plant with power of 1MWe coupled with a water production system was installed on the land and is capable of functioning productively compared to the investments required. A second market could be found in Guam and American Samoa with a land-based OTEC plant rated 10 MWe operating with an open cycle and embedding a second-stage water production system. A third market is located in Hawaii, where a larger and land-based OTEC system could produce electricity through a closed cycle. Its cost-effectiveness would be promoted by the high cost of diesel which is doubled in this market compared to the average for plants rated at least at 50 MWe. The fourth market is represented by floating plants with rated power equal to or greater than 40 MWe and operating with a closed cycle [7]. The original concept of the OTEC technology was proposed by J. A. d'Arsonval in 1881. Afterwards, the first demonstrative prototype of OTEC was built by his student G. Claude in 1928 in Belgium. In 1930, a prototype based on an open-cycle ORC was installed in a rocky natural pool in Cuba [8]. In the following years, the research efforts focused on realizing a large-scale OTEC plant but did not lead to remarkable achievements. In 1981, an on-shore pilot plant, working with a closed-cycle ORC and rated 100 kW was constructed by the TEPCO company in the Republic of Nauru [9]. In 2001, the National Institute of Ocean Technology of India and the Saga University of Japan installed an off-shore floating OTEC plant rated 1 MW connected to the grid [10]. The lack of funding retarded further projects until the beginning of the new millennium when the interest in ocean thermal energy conversion was renovated by the rise of the interest in renewable energy systems. In 2013, an OTEC plant with 100 kW of power and working with a closed cycle was built on the island of Kumejima in Japan and still operates effectively [11]. In 2015, an OTEC system rated 100 kW was built on Makai Island in Hawaii and was connected to the electric grid [8]. In the last years, relevant research was conducted for proposing systems integrating the OTEC technology with other renewable resource devices for energy transformation and storage [12–15]. The principal objectives are reducing the investment cost of individual devices by sharing the structure and infrastructure and developing comprehensive facilities for satisfying the needs of isolated communities [16,17]. A major problem of OTEC systems is transporting electric energy obtained to the grid, especially for floating offshore facilities. A solution to this problem could be using the electric energy transformed to obtain an energy carrier such as hydrogen. Indeed, its role will be crucial for the energy transition that will characterize the upcoming years due to the wide applicability and the absence of pollutant emissions during combustion. Moreover, the possibility of transforming hydrogen using renewable energy resources instead of reforming hydrocarbons provides substantial benefits for the environment. Some studies have assessed the production from renewable sources, as well explained in the review work of Nikolaidis et al. and Ishaq et al. [18,19], such as from biomass [20] and geothermal [21]. OTEC technology could also be employed. In this sense, Ahamdi et al. have proposed a multi-objective optimisation of an OTEC system for hydrogen production [22], Banarjee et al. have economically assessed the production of hydrogen with OTEC cycle [23], Ishaq compared the production of hydrogen from OTEC, wind and solar energy [24], Yilmaz et al. studied OTEC for hydrogen production [25,26], Soyturk evaluated the possibility to produce both hydrogen and distilled water from OTEC [27].

In this framework, the presented research aims to evaluate the use of electric energy converted by an OTEC system to operate an electrolyzer that shifts the water into hydrogen and oxygen in the electrolysis process. The hydrogen gas is compressed and stored in storage systems to facilitate transport. The hydrogen production system is integrated with a solar collector to maximize the use of renewable energies. Indeed, the collector supplies the heat required to warm up the seawater to the working temperature of the electrolyzer. Exergy and exergo-economic analyses were conducted for three suitable configurations of the OTEC cycle considering the Kalina cycle, the Rankine cycle with a water-ethanol mixture and the Rankine cycle with ammonia. The performance and techno-economic key indicators were determined and compared between themselves and with other technical solutions.

2. Materials and methods

The schematic of the energy system investigated is illustrated in Fig. 1. The main components are a desalination device, a solar collector providing the thermal power for heating the oceanic water, and the OTEC system producing the electricity powering the pumps, the electrolyzer and the compressor used to store hydrogen. The plant is capable of converting 1 MW of electric power through the OTEC cycle.

The assumptions applied for the system modelling are listed in the following:

1. The system operates under steady-state conditions.
2. The ambient temperature and pressure are assumed equal to 288.15 K and 101.325 kPa, respectively.
3. The pressure drops in the heat exchangers are negligible except for the OTEC cycle.
4. The changes in the kinetic and potential energies are negligible.

2.1. Desalination system

A preliminary desalination treatment was considered as the electrolyzer is not able to operate with seawater [28]. This system consists of a Reverse Osmosis (RO) group placed at the inlet of the plant. This choice was made as Reverse Osmosis is a very consolidated desalination technology utilised in the majority of the desalination plants installed worldwide [29–32]. Moreover, RO plants have a wide range of values of average capacity for desalinated water production [30]. The configuration of the RO system implemented is composed of the components listed below [33]:

1. A feed water supply unit, which takes the water from the sea and brings it to the plant.
2. A pre-treatment section with filtration, flocculation, and clarification process, which prevents some complications to the functioning of the membranes.
3. A high-pressure pumping unit, that ensures reaching the design pressure level.
4. A membrane unit that removes the dissolved salt from the water, generating the desalinated stream and the rejection stream.
5. A rejection stream treatment, which limits the environmental impacts of the reinjection in the sea.

Fig. 2 shows a standard RO desalination system. In this paper, the desalination system is modelled as a "black box", evaluating the recovery rate, as introduced in Equation (1), the standard energy consumption, and the standard capital and operation costs [29–31,34]. Considering that the range of energy consumption of a RO desalination system is between 3.0 and 6.0 kWh/m^3, an electricity requirement of 4.5 kWh/m^3 was assumed. The value of 1500.0 \$/m^3 was considered for the capital cost of the desalination system.

The recovery rate of the desalination system is expressed through Eq.

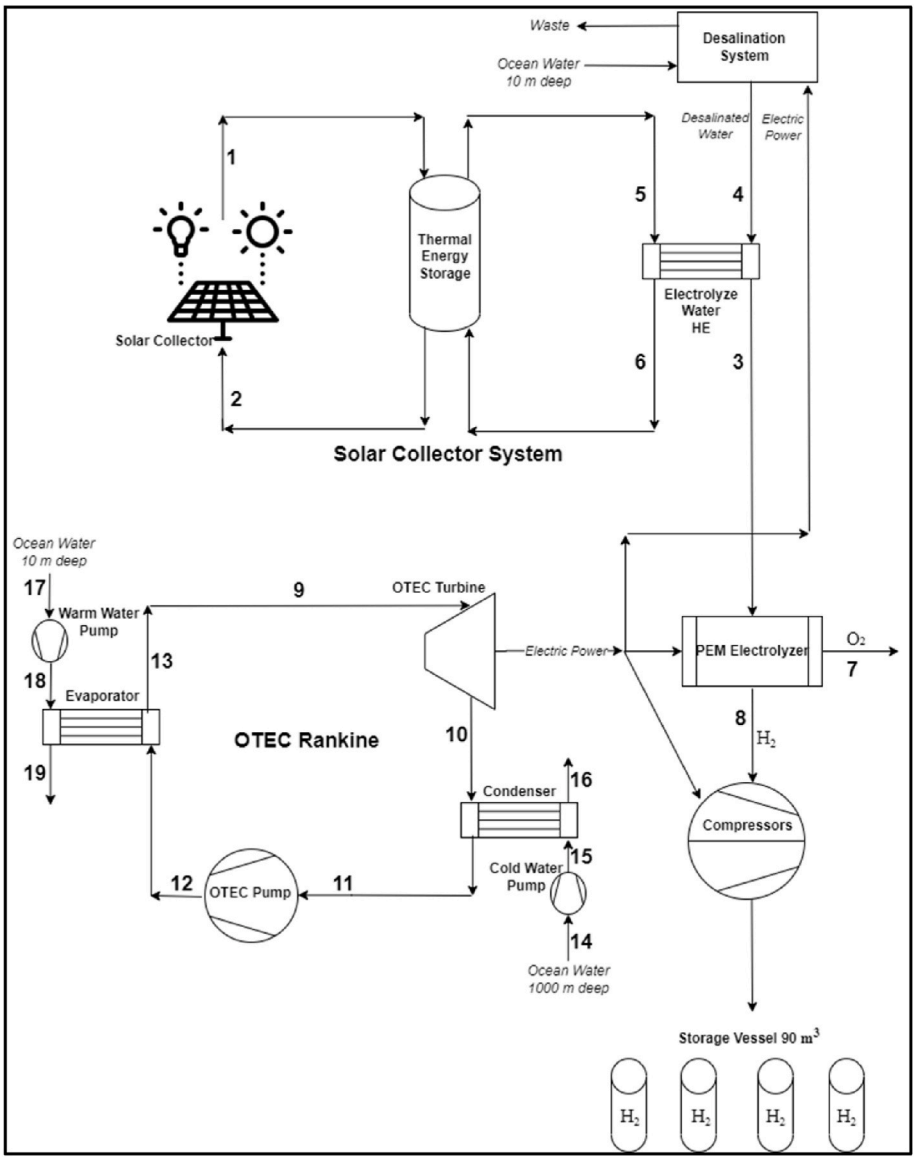

Fig. 1. Scheme of the analysed power plant.

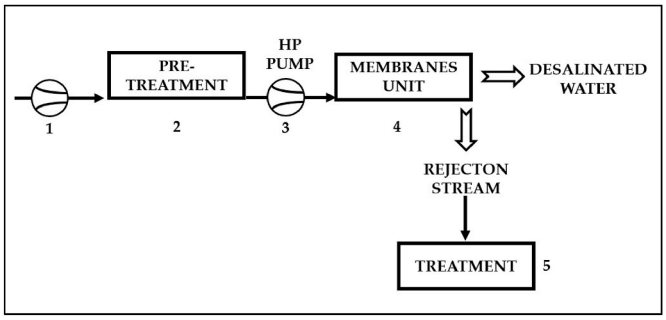

Fig. 2. Scheme of a standard desalination system with reverse osmosis.

(1).

$$RR = \frac{Produced\ desalinated\ water}{Inlet\ water} \quad (1)$$

Considering a common value for the recovery rate [34] and the necessary desalinated mass flow rate equal to the design mass flow rate of the electrolyzer, the supply of seawater and the production of permeate were defined as indicated in Table 1.

2.2. Solar collector system

The principal components of the solar system are the solar collectors, the thermal storage, and the surface heat exchanger with separate flows (Fig. 3). The operating fluid for the solar collector is the Therminol VP1. The thermal energy storage (TES) was included to provide a constant temperature of 105 °C to the water despite the variable radiation gathered by the solar collector during the day.

The solar cycle analysis is carried out for a site positioned in Brazil (S 5°, W 36°), where the ocean profile temperature is attractive for OTEC application. Fig. 4 provides the temperature profile of the ocean water in

Table 1
Recovery rate of the device.

Recovery rate	0.50	–
Inlet seawater mass flow rate	0.0428	kg/s
Desalinated mass flow rate	0.0214	kg/s
Rejection stream mass flow rate	0.0214	kg/s

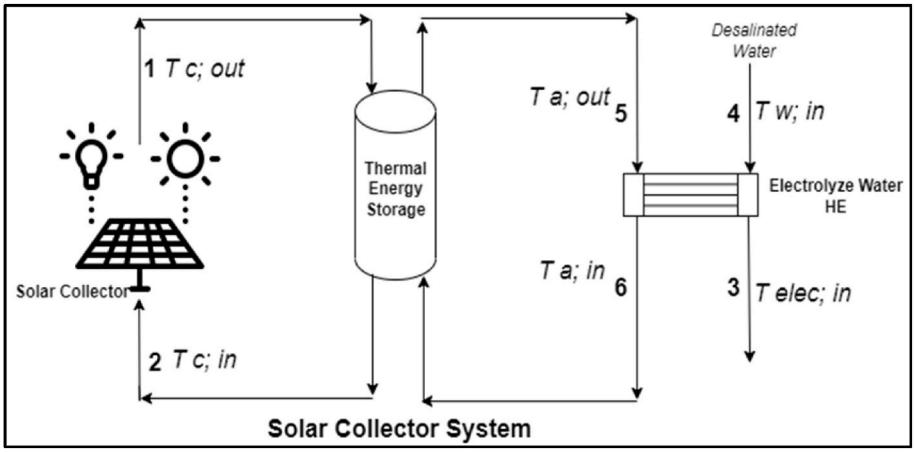

Fig. 3. Scheme of the analysed solar collector device.

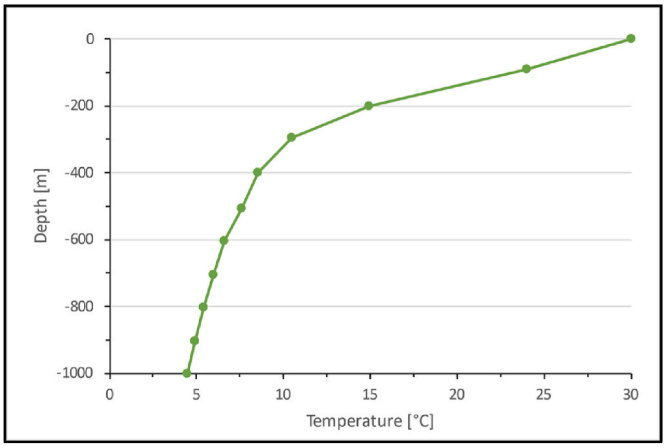

Fig. 4. Oceanic water temperature for sea depth.

this location [3].

The data of the total radiation G, the direct radiation G_d and the ambient temperature was obtained by the software PVGIS on an annual basis [35]. The data defining the configuration of the solar collectors are resumed in Table 2.

The collector efficiency is calculated with Eq. (2) based on the total radiation on the tilted surface G_T, and the average temperature difference between the solar collector and the environment ΔT_a.

$$\eta_c = c_0 - c_1 * \frac{\Delta T_a}{G_T} - c_2 * \frac{\Delta T_a{}^2}{G_T} \tag{2}$$

The parameters assumed for determining the collector efficiency curve are listed in Table 3.

The collector efficiency is assumed to be equal to zero when the radiation is absent. The total radiation G_T is calculated using the Liu-Jordan correlation of Eq. (3).

$$G_T = G_b * R_b + G_d * \frac{1 + cos\ cos\ (\beta)}{2} + (G_b + G_d) * \frac{1 - cos\ (\beta)}{2} * \rho_g \tag{3}$$

Table 2
Specifications of the solar collectors.

Tilt angle of the surface on the horizontal plane	β	32°
Surface azimuth angle	γ_{az}	0°
Shallow ocean water temperature inlet (10 m depth)	T_{wi}	29.56 °C
Land surface reflectance	ρ_g	0.2

Table 3
Solar collector characteristic curve parameters.

Parameter	Value	Unit
c_0	0.741	–
c_1	0.043	W/(m^2 K)
c_2	0.00050256	W/(m^2 K^2)

where R_b is the ratio between the incidence angle of the direct radiation on the inclined surface and the zenith angle of the sun.

In the solar collector system, there are three different mass flow rates: the main stream of Therminol VP1 $\dot{m}_c$ circulating in the solar collector, the secondary stream of Therminol VP1 $\dot{m}_{stor}$ provided by the thermal energy storage device and the water $\dot{m}_s$ warmed in the heat exchanger. The mass flow rate $\dot{m}_c$ was calculated based on the typical design value of 50 l/h/m^2. The water mass flow rate $\dot{m}_s$ was obtained by solving the energy balance of the electrolyzer, assuming the nominal value of the input electric power of 1 MW. The mass flow rate $\dot{m}_{stor}$ was determined through the energy balance of the solar collector system. An iterative analysis was performed to evaluate the variation of the thermal loads and the temperature inside the TES device due to the variability of heat gathered by the solar collector during days and months. This analysis allows for defining the correct value of $\dot{m}_{stor}$ during the whole operation. The thermal power necessary for heating seawater from the inlet temperature $T_{w;in}$ to the temperature $T_{elect;in}$ of 80 °C required by the PEM electrolyzer are provided by Eq. (4) and Eq. (5) for the i-th hour of the day.

$$\dot{Q}_{HE}[i] = \dot{m}_s * c_{p;water}[i] * \left(T_{elect;in} - T_{w;in}\right) \tag{4}$$

$$\dot{Q}_{HE}[i] = \dot{m}_{stor}[i] * c_{p;VP1}[i] * \left(T_{a;out}[i] - T_{a;in}[i]\right) \tag{5}$$

The heat power instantaneously accumulated by the solar collector $\dot{Q}_{collector}$ is computed with Eq. (6) relying on the collector efficiency.

$$\dot{Q}_{collector}[i] = \eta_c[i] * G_T[i] * A_c \tag{6}$$

The heat loss from the storage to the environment Q_{loss} is expressed in Eq. (7). The value of the product between the global heat transfer coefficient and the heat transfer area UA was assumed equal to 0.011 kW/°C.

$$\dot{Q}_{loss}[i] = UA * \left(T_{a;out}[i] - T_{amb}[i]\right) \tag{7}$$

The final reasonable storage capacity results in 5000 kg. The solar collector area A_c was defined to guarantee the correct functioning of the plant throughout the year, especially during June, that is the most critical month for the selected location. Finally, the global efficiency of

the solar collector was determined with Eq. (8):

$$\eta = \dot{m}_s * \frac{h_{w,out} - h_{w,in}}{\dot{Q}_{collector}} = 1 - \frac{\dot{Q}_{loss} + \dot{Q}_{stor}}{\dot{Q}_{collector}} \quad (8)$$

2.3. OTEC

Three different configurations of an OTEC system with 1 MWe of net power output were analysed. This choice for the power is in line with the work of Aresti et al. [36]. Generally, an increase in the size corresponds to a decrease in the cost of electricity production, as well explained by Vega et al. [37].

In the first one, a Rankine cycle with ammonia as the working fluid is used; in the second configuration, the working fluid is a mixture of water and ethanol with mass fractions of 80% and 20%, respectively; in the last layout, a Kalina cycle with an ammonia mass fraction of 82% is utilised. The OTEC configuration extracts the warm seawater in the proximity of the surface for heating the fluid in the evaporator. Conversely, the cold seawater is taken around 1000 m below the surface level to cool the working fluid in the condenser. With this configuration, the binary cycle is able to operate between 29.5 °C and 4.5 °C. The Carnot efficiency for this range of temperatures is about 8%. Fig. 5 shows a schematization of the OTEC Rankine power plant, highlighting the binary cycle and the hot and cold fluid pipelines feeding the evaporator and the condenser, respectively. The working fluid, vaporized by the warm oceanic water, expands in the turbine before being condensed by the cold seawater in the condenser. The condensed working fluid is then pumped into the evaporator.

Fig. 6 shows the layout of the OTEC power plant with the Kalina cycle. In this case, the zeotropic working fluid enters a separator once it is vaporized. The rich ammonia mixture is then expanded in the turbine, while the weak ammonia solution preheats the basic composition mixture in a recuperator, and it is subsequently laminated in a valve and mixed with the strong solution exiting the turbine. After the mixer, the solution is condensed by the cold seawater. A low-temperature recuperator is utilised to improve the efficiency of the cycle.

The specifications of the systems functioning with the Rankine and Kalina cycles are summarized in Table 4.

The mass and energy balances of the system were solved based on the ratio between the mass flow rate of cold and warm water γ. In particular, Eq. (9) and Eq. (10) refer to the Rankine cycle and Eq. (11) and Eq. (12) to the Kalina cycle.

$$\dot{Q}_{eva} = \dot{m}_H(h_{18} - h_{19}) = \dot{m}_{WF}(h_{13} - h_{12}) \quad (9)$$

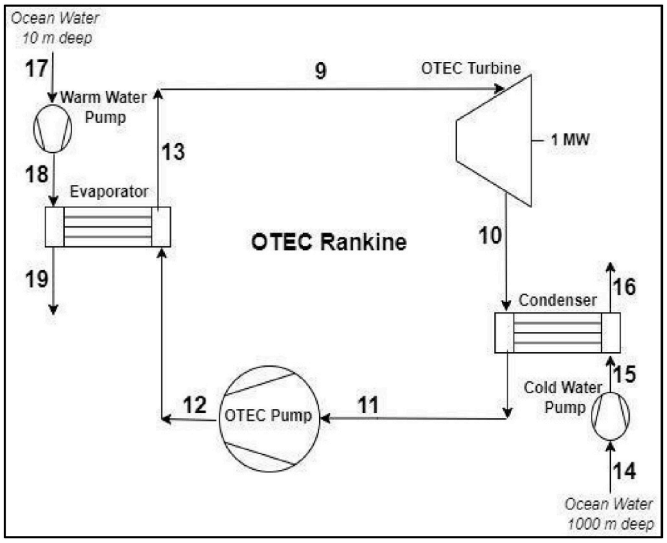

Fig. 5. Schematic of OTEC power plant with the Rankine cycle.

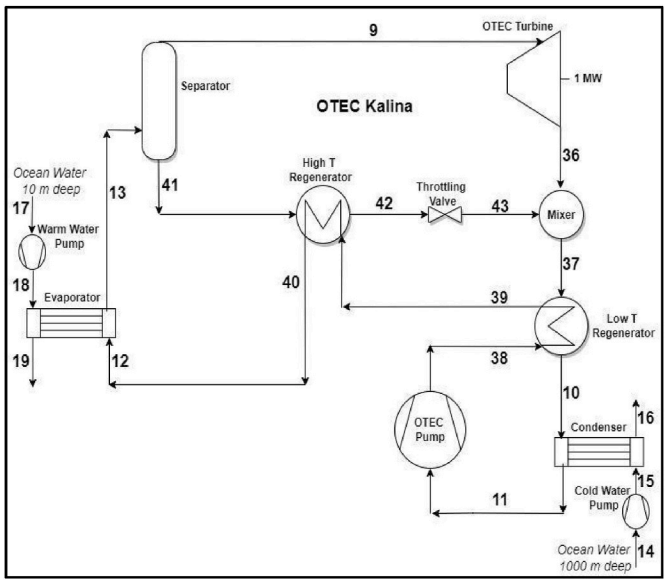

Fig. 6. Schematic of OTEC power plant with Kalina cycle.

Table 4
Specifications of the OTEC systems operating with the Rankine and Kalina cycles.

Parameter	Rankine		Kalina	
	Value	Unit	Value	Unit
Turbine isoentropic efficiency	90	%	90	%
Pump isoentropic efficiency	90	%	90	%
Net power output	1000	kW	1000	kW
Condenser range	5	°C	2.2	°C
Mass flow rate of cold and warm water ratio (γ)	0.65	–	1.3	–

$$\dot{Q}_{cond} = \dot{m}_C(h_{16} - h_{15}) = \dot{m}_{WF}(h_{10} - h_{11}) \quad (10)$$

$$\dot{Q}_{eva} = \dot{m}_H(h_{18} - h_{19}) = \dot{m}_{WF}(h_{13} - h_{12}) \quad (11)$$

$$\dot{Q}_{cond} = \dot{m}_C(h_{16} - h_{15}) = \dot{m}_{WF}(h_{10} - h_{11}) \quad (12)$$

The pressure losses of the heat exchangers were calculated based on the total pressure loss given by the sum of the pressure losses at the inlet, plate, port and tubes. The pressure loss ΔP_{inlet} due to the entrance in the heat exchanger was calculated using Eq. (13).

$$\Delta P_{inlet} = \frac{K * w_{mean}^2 * \rho_w}{2} \quad (13)$$

where K is a parameter considering the geometry of the inlet and depends on the diameters of the pipe and the tube of the heat exchanger, w_{mean} is the mean velocity of water in the tubes and ρ_w is the water density.

The pressure drop ΔP_{plate} along the heat exchanger plate is provided by Eq. (14) relying on the friction factor f in the plate and the length L_p and hydraulic diameter D_h of the plate.

$$\Delta P_{plate} = \frac{4f * \rho_w * w_{mean}^2 * L_p}{2 * D_h} \quad (14)$$

The pressure loss ΔP_{ports} at the heat exchanger inlet ports was determined by Eq. (15) based on the mass flow rate of seawater $\dot{m}$ and the pipe diameter D_{pipe} of the heat exchanger.

$$\Delta P_{ports} = 1.4 * \left(\frac{4\dot{m}}{\pi * D_{pipe}^2}\right)^2 * \frac{1}{2\rho_w} \quad (15)$$

The pressure drop ΔP_{pipe} along the heat exchanger pipes was computed with Eq. (16) as a function of the friction factor f_{pipe} and the length L_{pipe} of the pipings.

$$\Delta P_{pipe} = 2 f_{pipe} * \frac{L_{pipe}}{D_{pipe}} * \rho_w * w_{mean}^2 \tag{16}$$

The total pressure drop in the water pumping systems was determined through Eq. (17) considering the depth of extraction and reinjection of water $depth_{extr}$ and $depth_{reinj}$, respectively.

$$\Delta P_{pipe} = \frac{f_{pipe} * \left(depth_{extr} + depth_{reinj} \right) * \rho_w w_{mean}^2}{2 D_{pipe}} \tag{17}$$

The depth of reinjection was defined according to the temperature profile of Fig. 4. The total pressure drop of the water cold circuit was found as the sum of the pressure loss of the condenser and the pressure loss of the cold water pumping system, while the total pressure drop of the hot water circuit was determined as the sum of the pressure loss of the evaporator and the warm pumping system.

The global efficiency of the OTEC cycle was calculated with Eq. (18) as the ratio between the net power output and heat provided at the evaporator.

$$\eta = \frac{\dot{W}_{net}}{\dot{Q}_{Eva}} \tag{18}$$

2.4. Electrolyzer

A Polymer Electrolyte Membrane (PEM) electrolyzer is used to produce hydrogen and oxygen by converting electricity and water. The overall reaction occurring in the electrolyzer is stated by Eq. (19). This technology is selected due to its fast dynamic response and wide operating power ranges. These features determined the preference over a common alternative, the alkaline fuel cell (AFC) system.

$$H_2O + energy \rightarrow H_2 + \frac{1}{2} O_2 \tag{19}$$

The reactions in the anode and cathode are listed in Eq. (20) and Eq. (21), respectively.

$$H_2O \rightarrow 2H^+ + \frac{1}{2} O_2 + 2e^- \tag{20}$$

$$2H^+ + 2e^- \rightarrow H_2 \tag{21}$$

The electric energy input rate is provided by the product of the current density J and the electrolyzer voltage V that is given by the sum of the reversible potential V_0, the electrolyte ohmic overpotential V_{ohm} and the activation overpotential of the cathode and anode $V_{act,c}$ and $V_{act,a}$, respectively. The reversible potential is determined with Eq. (22) by applying the Nernst formula.

$$V_0 = 1.229 - 8.5 \times 10^{-4} (T_{PEM} - 298) \tag{21}$$

The ohmic overpotential across the proton exchange membrane is caused by its resistance to the passage of the hydrogen ions. The main factors impacting the ionic resistance of the membrane are the humidification degree, the membrane thickness and temperature. The ohmic overpotential was calculated using Eq. (22).

$$V_{ohm} = J R_{PEM} = \int_0^L \frac{dx}{\sigma[\lambda(x)]} \tag{22}$$

The local ionic conductivity of the membrane $\sigma[\lambda(x)]$ was determined with Eq. (23).

$$\sigma[\lambda(x)] = [0.5139\lambda(x) - 0.326] exp\left[1268 \left(\frac{1}{303} - \frac{1}{T} \right) \right] \tag{23}$$

The variable x is the depth in the membrane from the cathode membrane interface, and $\lambda(x)$ is the water content in position x on the membrane. The value of $\lambda(x)$ in terms of water content at the anode-membrane λ_a and the cathode-membrane λ_c was defined with Eq. (24) based on the membrane thickness L.

$$\lambda(x) = \frac{\lambda_a - \lambda_c}{L} x + \lambda_c \tag{24}$$

The activation overpotential V_{act} of the cathode and anode were calculated using Eq. (25).

$$V_{act,i} = \frac{RT}{F} sin\, h^{-1} \left(\frac{J}{2 J_{0,i}} \right), i = a, c \tag{25}$$

The exchange current density J_0 is provided by Eq. (26).

$$J_{0,i} = J_i^{ref} \, exp\left(- \frac{E_{act,i}}{RT} \right), i = a, c \tag{26}$$

Assuming the ideal gas behaviour and neglecting the side reactions, the mass flow rate of the hydrogen and oxygen was computed using Eq. (27) and Eq. (28), respectively, relying on the molecular weight MM and the Faraday constant F. The required mass flow rate of water was defined by the sum of the mass flow rates of hydrogen and oxygen.

$$\dot{m}_{H_2} = \frac{J}{2F} MM_{H_2} \tag{27}$$

$$\dot{m}_{O_2} = \frac{J}{4F} MM_{O_2} \tag{28}$$

The global efficiency of the electrolyzer is provided by Eq. (29) as a function of the lower heating value LHV_{H_2} of the hydrogen.

$$\eta = \frac{LHV_{H_2} \dot{m}_{H_2}}{\dot{W}} \tag{29}$$

2.5. Compression and storage

The compression system enables the storage of hydrogen in tanks with a volume of 90 m^3 at a pressure of 300 bar. This transformation is fundamental to ease the storage of hydrogen in a reasonable volume as the electrolyzer provides hydrogen at 30 bar.

The system illustrated in Fig. 7 is composed of a pre-cooler, 3 compressor stages and 3 after-coolers. The possible recovery of the water in the coolers is not considered and it is consequently treated as a loss.

The isentropic efficiency of the compressors was assumed equal to 0.86 and the rotational speed of the compressors was equivalent to 1500 rpm. The pressure ratio of the compression stage was calculated as the ratio between the pressure of the stored hydrogen and the inlet hydrogen [38].

2.6. Exergy analysis

The exergy analysis allows the evaluation of the source of the irreversibility of the system and of each component composing it. To this end, the exergy destruction and losses of each component are calculated.

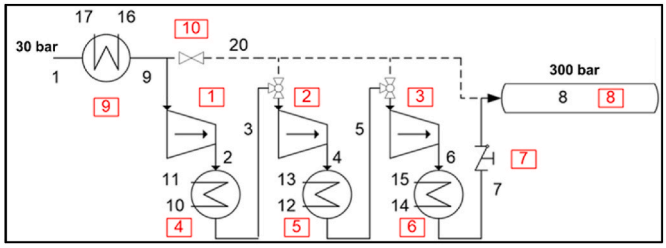

Fig. 7. Scheme of the system for hydrogen compression and storage.

The total physical exergy of a stream is calculated at every point of the thermodynamic cycle by applying Eq. (39).

$$ExT_{t,ph} = \dot{m}[(h - h_0) - T_0(s - s_0)] \quad (39)$$

At the component level, there is a substantial difference between exergy destruction and exergy loss. The exergy destruction is due to different possible irreversibilities within a thermodynamic transformation such as friction, heat transfer in a defined control volume with finite temperature difference. The exergy loss is associated with exergy transfer wasted to the surroundings. In the supplementary materials, the equations utilised to calculate the exergy destructions and losses of every component are summarized. For the electrolyzer, the chemical exergy is also considered, because of the chemical hydrolysis reaction. The chemical exergy of a stream is calculated with Eq. (40).

$$ExT_{t,ch} = \dot{m}\frac{Ex_{st,ch}}{MM} \quad (40)$$

where $ExT_{st,ch}$ is the standard chemical exergy and MM is the molar mass of the considered molecule.

Finally, the exergy efficiency of the system can be calculated with a direct procedure as the ratio between the product total exergy and the fuel total exergy, or with an indirect procedure as the complement to 1 of the ratio between the sum of exergy destructions and losses of each component and the fuel input total exergy.

The indirect formulation of the exergy efficiency of Eq. (41) allows the comparison of the different sources of irreversibilities.

$$\eta_{ex} = \frac{ExT_{out}}{ExT_{in}} = 1 - \frac{\sum ExD_k + \sum ExL_k}{ExT_{in}} \quad (41)$$

The equations used for the exergy efficiency of the single system are summed in Table 5.where ExT_{coll} is the exergy of the heat captured by the solar collector, calculated as the product of the heat collected and the Carnot factor (θ); ExT_{TES} is the exergy stored in the thermal energy storage, computed as the product of the heat stored for the Carnot factor; GJ is the geodetic head, determined through Eq. (42).

$$GJ = \dot{m}_c(h_{20} - h_{21}) + \dot{m}_H(h_{10} - h_{14}) \quad (42)$$

2.7. Exergo-economic analysis

The exergo-economic analysis combines the exergy and economic analyses to find the cost build-up through the power plant process. For this type of analysis, an estimation of the cost of every component is required. Therefore, several cost correlations were considered to select the best-suited ones by analysing their validity range. The list of the correlations used to obtain the purchase equipment cost (PEC) of the components is reported in the supplementary materials. The correlations refer to the prices of the year of their publication and were actualized to the values of 2022 using the CEPCI indexes [39].

To evaluate the cost of the heat exchangers, the calculation of the surface of these components is required. The surface is calculated with Eq. (43) assuming a proper value of the global heat transfer coefficient U.

$$A_{HE} = \frac{\dot{Q}}{U^* \Delta T_{ML}} \quad (43)$$

where ΔT_{ML} is the log mean temperature of the heat exchanger.

The values of the global heat transfer coefficient listed in Table 6 are taken from Refs. [40,41].

From the total PEC of every component, the total capital investment (TCI) is obtained considering also all the other related costs (such as installation, piping, etc.), as suggested in Ref. [42]. The TCI is utilised to calculate the annual instalment (AI) through Eq. (44):

$$AI = TCI^* \frac{ir^*(1+ir)^n}{(1+ir)^n - 1} [€] \quad (44)$$

where ir is the interest rate and n is the lifespan of the plant. Their values were chosen respectively equal to 7.5% and 25 years according to Khosravi et al. [43]. Then, the AI is summed with the operation and maintenance costs (O&M), which are hypothesized equal to 5% of PEC [43,44] to obtain the total power plant cost.

The capital cost of every component is provided by Eq. (45):

$$\dot{Z}_k = \frac{Total\ Power\ Plant\ Cost^* PEC_k}{PEC_{totale}^* Nh^* 3600} \left[\frac{€}{s}\right] \quad (45)$$

where N_h is the number of the operating hours of the power plant, assumed as 8000 h.

After the determination of the capital costs of each component, the exergo-economic approach can be deployed through Eq. (46), which provides a cost balance equation for each component k [45].

$$c_{p,k} ExT_{p,k} = c_{f,k} ExT_{f,k} + \dot{Z}_k \quad (46)$$

where $c_{p,k}$ and $c_{f,k}$ are the costs per unit of the exergy of the product or fuel, respectively. In this analysis, the cost of exergy losses is considered at zero, while other auxiliary equations needed to solve the system are taken from the literature [45].

3. Results and discussions

3.1. Solar collector

The overall efficiency of the solar collector is 45% under design conditions. It decreases with increasing the collector area, as shown in Fig. 8 (a). This is not due to a degradation of the collector performance but to the required constant amount of power output. As the heat provided to the water is unchanged, part of the heat entering the solar collector is dissipated. Indeed, the inlet power increases with increasing the solar collector area. Fig. 8 (b) shows the marginal dependence of the global efficiency on the storage's initial (morning) temperature. This choice affects directly only the heat loss to the environment, which has a low impact on global efficiency.

Since the heat captured by the solar collector was considered as the input energy in place of the ideal value of the radiation, the levels of exergy destruction of the solar collector are negligible compared to the other components of the system, as shown in Fig. 9. The obtained exergy efficiency of the solar system resulted at about 14.6%.

Table 5
Equations for exergy efficiencies.

SYSTEM	EQUATION
Solar collector	$\eta_{ex} = \frac{ExT_3 - ExT_4}{ExT_{coll} + ExT_{TES}}$
OTEC	$\eta_{ex} = \frac{GJ + \dot{W}_{net}}{(ExT_{hw} - ExT_{19}) + (ExT_{cw} - ExT_{16})}$
Electrolyzer	$\eta_{ex} = \frac{ExT_8}{\dot{W}_{net} + ExT_3}$

Table 6
Global heat transfer coefficient of the different heat exchangers [28,29].

COMPONENT	U [W/m^2 K]
Electrolyze water HE	150
OTEC condenser	1000
OTEC evaporator	1000
High T regenerator	1000
Low T regenerator	1000
Coolers	100

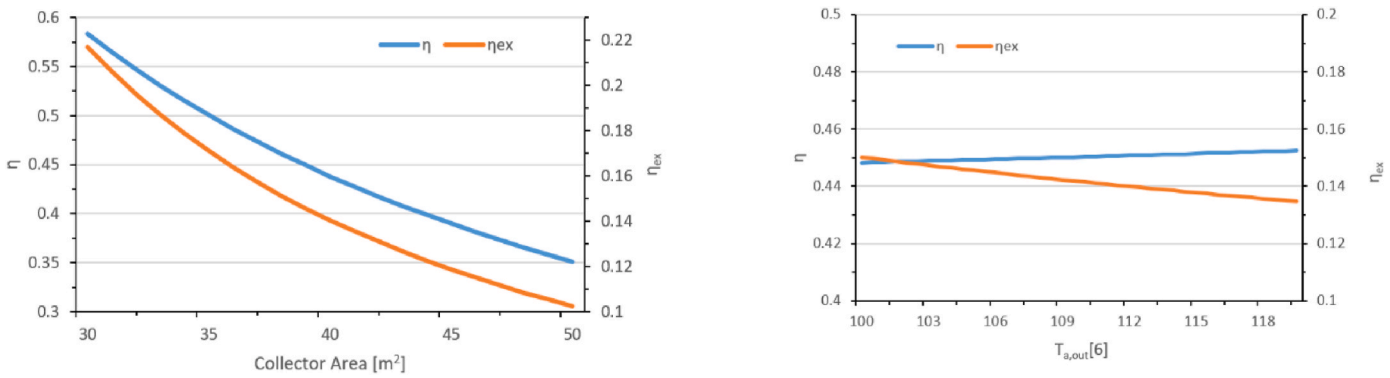

Fig. 8. Global efficiency of the solar cycle as a function of the collector area (a, left) and the TES initial temperature (b, right).

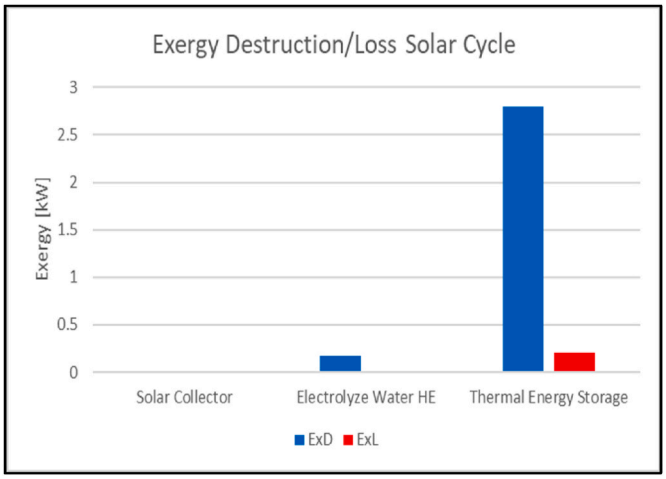

Fig. 9. Exergy destructions and losses of solar cycle components.

3.2. OTEC cycle

In Table 7, the amounts of total pressure drops of the water circuits are resumed. In each cycle configuration, the major losses occur in the cold circuit as its length is markedly longer than the hot circuit because of deep ocean extraction.

Fig. 10 shows that the net-specific work produced by the system has a maximum function of the mass flow rate in the cold pipe of both Rankine and the Kalina cycle configurations. This value is obtained by the combination of the opposite effects of the gross power of the turbine and the required pumping power, necessary to overcome the pressure losses in the pipes.

For the Rankine cycle, a parametric analysis was carried out with variable water mass flow ratio γ and condenser range to find the optimal efficiency values. Fig. 11 shows that the efficiency is mostly influenced by the condenser range and increases with its reduction. This is mainly due to the increase in the thermodynamic efficiency of the power cycle, which allows lower values of condensing temperature [3].

Table 7
Values of pressure drop of water circuits in the OTEC cycle.

Rankine Ammonia	ΔP [kPa]
ΔP_{hot}	5.78
ΔP_{cold}	19.67
Rankine water-ethanol	
ΔP_{hot}	24.93
ΔP_{cold}	40.82
Kalina	
ΔP_{hot}	4.73
ΔP_{cold}	21.86

For the Rankine cycle with the water-ethanol mixture, the variation of the global efficiency with the water mass fraction was also analysed. Fig. 12 shows the sensitivity of the efficiency to the water mass fraction, which is negligible compared to the water mass flow ratio γ.

For the Kalina cycle, the global efficiency and the exergy efficiency were parameterized on the ammonia mass fraction in the basic solution. As shown in Fig. 13, the maximum efficiency is achieved for values of mass fraction between 84% and 87%, and the maximum exergy efficiency is obtained for a mass fraction of about 86%.

In all the analysed configurations, the global efficiency is very low, because the power cycle works between 29.5 °C and 4.5 °C. With the considered input data, the Rankine cycle has a global efficiency of 3.77% with ammonia and 3.80% with the water-ethanol mixture, while for the Kalina cycle, the efficiency is 3.58%, which are encouraging values, considering that an 8% Carnot maximum efficiency is achievable within the considered temperature boundaries.

For the exergy analysis, the contribution of the individual components to the exergy destructions and losses are reported in Fig. 14 for the different configurations analysed.

The transformations most largely affecting the efficiency reduction are the condenser and the evaporator, in all the configurations. This is due to the non-optimal thermal matching between the working fluid and the oceanic water. As suggested in Ref. [3], this destruction has been reduced in this work by using dedicated zeotropic mixtures with suitable temperature glides. As expected, the Kalina cycle is the one with the lowest irreversibility in the heat exchangers. No exergy losses were considered, as the discharge of the heated cold flow rate and that of the cooled but still warm stream at the evaporator output represent conditions imposed by the plant operation [3].

Under design conditions, the exergy efficiency is 93.0% for the Rankine cycle with ammonia, 92.4% for the Rankine cycle with a water-ethanol mixture, and 95.9% for the Kalina cycle.

A sensitivity analysis has been carried out for the investigation of the exergy efficiency. For the Rankine cycle, Fig. 15 displays the effects of the water mass flow ratio and the condenser range on the second law efficiency. The highest values of exergy efficiency are achieved corresponding to the lower levels of the condenser range, similar to the behaviour of global efficiency. This is due to a reduction in the exergy destruction of this system.

3.3. Electrolyzer

An important aspect of electrolyzers is the sensitivity of the voltage to the current density. Fig. 16a displays this behaviour achieved with the calculation model here proposed and it is in agreement with the typical value of the PEM electrolyzer obtained with experimental data [46]. Fig. 16b) shows the behaviour of global and exergy efficiency with

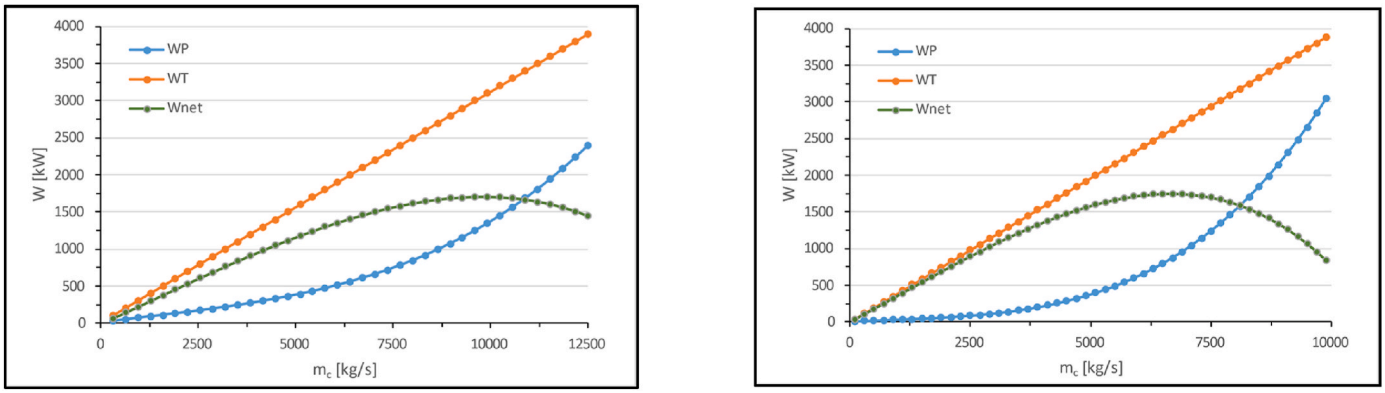

Fig. 10. Net and gross power of the turbine and power required by the pumps in OTEC Rankine cycle (a) and Kalina cycle (b).

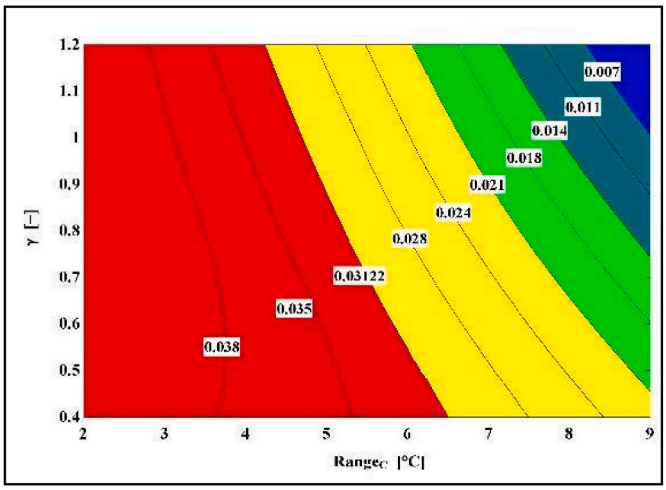

Fig. 11. Isolines of global efficiency as functions of the water mass flow ratio and the condenser range.

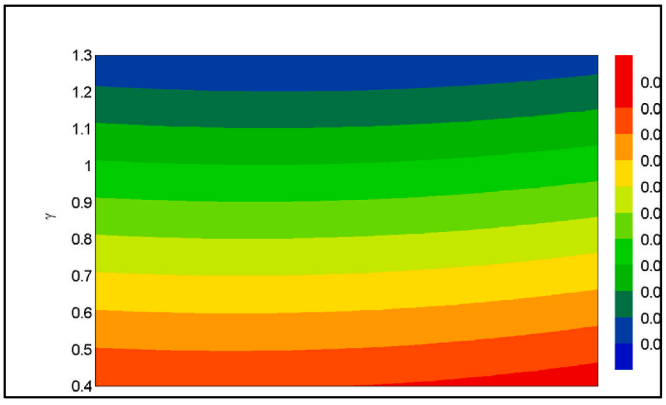

Fig. 12. Isolines of global efficiency as functions of the water mass flow ratio and the water mass fraction.

current density. Efficiencies have similar values and the same behaviour; both efficiencies decrease as current density rises. Indeed, as can be noted from the comparison between Fig. 16a) and b), the efficiency of the electrolyzer is inversely proportional to the voltage.

The electrolyzer is fed by the electricity output from the OTEC cycle. In all the configurations, the 1 MW nominal electric power drives the electrolyzer, the compressors, and the desalination plant (which however has a negligible power consumption of about 350 W). Therefore, as

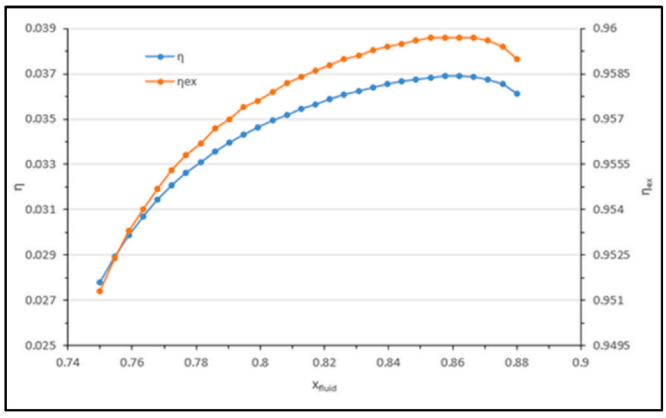

Fig. 13. Global efficiency and exergy efficiency versus ammonia mass fraction.

the compressors require 10 kW power, 990 kW are provided to the electrolyzer. At this value of available power, the results are summarized in Table 8.

From the sum of hydrogen and the oxygen mass flow rate, the 0.02141 kg/s water mass flow rate required through the solar collector is achieved. The hydrogen mass flow rate produced in a day is 205.5 kg.

For the exergy analysis, the oxygen mass flow rate is considered a loss, as the use of oxygen is not taken into account. The exergy destructions and losses are respectively 709.3 kW and 4.955 kW. The global efficiency of the component is 28.8%, while the exergy efficiency is 29%.

3.4. Compression and storage

The pressure ratio of each stage is 2.154. Each compressor is driven by the electricity of the OTEC cycle, and the power of each compressor is about 3 kW.

The results of the exergy analysis of the hydrogen compression and storage are reported in Fig. 17. For the coolers, possible re-use of the cooling water is not considered, which thus represents an exergy loss. Another exergy loss is represented by the heat dissipation to the environment in the filling stage.

The global and exergy efficiency results respectively equal 33.5% and 73.4%.

3.5. Exergo-economic analysis

The OTEC is the most impacting device on the thermo-economic aspects of the entire system. Particularly, Fig. 18 shows the share of every single system in overall purchase equipment cost. The pie chart

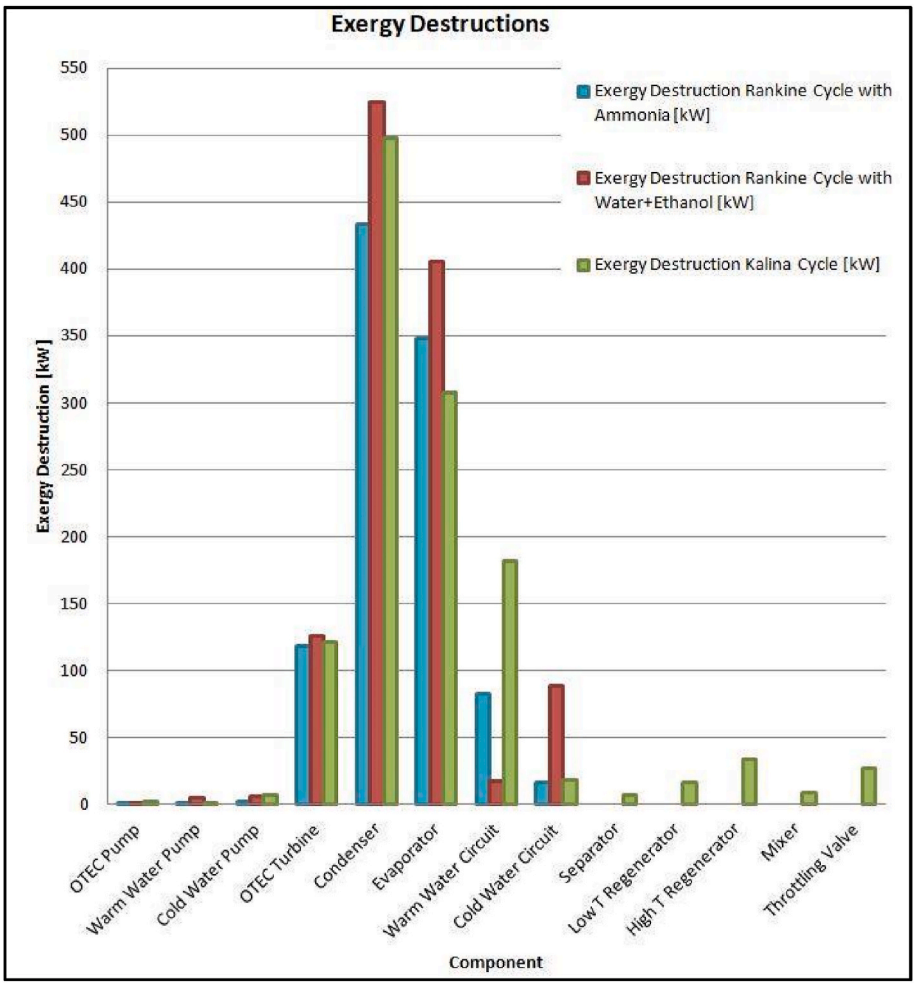

Fig. 14. Exergy destructions and losses for the OTEC Rankine cycles with ammonia, water-ethanol mixture, and for the OTEC Kalina cycle.

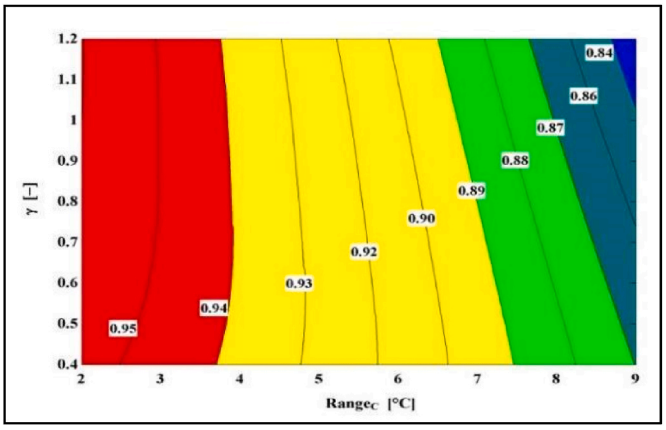

Fig. 15. Isolines of exergy efficiency to changes in the water mass flow ratio and the condenser range.

refers to the Rankine cycle with ammonia, but it is representative of all the analysed configurations.

Fig. 19 splits the contribution of the total cost of the OTEC (a) and the compression and storage system (b). For the OTEC, the condenser and the evaporator are the most expensive components, followed by the turbine, as shown in Fig. 19 (a). For the compression and storage system, the vessel plays a major role, followed by the various coolers, while the compressors play a minor role.

The obtained overall specific investment cost of the whole system is 13283 €/kW.

Table 9 shows the results obtained from the exergo-economic analysis related to the operation of the system in the base case.

From the exergo-economic analysis, if $\dot{Z}_k$ and $\dot{C}_{D,k}$ are summed, the PEM electrolyzer, the condenser, and the evaporator are the most important components. However, other components with relevant contributions in terms of exergy destruction costs $\dot{C}_{D,k}$ also emerged. They are represented by the turbine and the various after-coolers.

One of the aims of the exergo-economic analysis of the OTEC cycle is to determine the cost of electricity production. It results in 26.4 c€/kWh for the Rankine cycle with ammonia, 23.6 c€/kWh for the Rankine cycle with the water-ethanol mixture, and 13.8 c€/kWh for the Kalina cycle. These values are high compared to the other RES, even though the Kalina shows a strong improvement over the two Rankine cycle configurations.

After the calculation of the OTEC electricity cost, it is possible to evaluate the cost of the produced hydrogen. This is, as expected, strongly dependent on the considered OTEC cycle, as it mainly depends on the cost of the electric power. So, as the Kalina cycle shows the lowest cost of electricity, the cost of the related produced hydrogen is the lowest, as shown in Fig. 20.

Finally, Table 10 reports the cost of the produced, compressed, and stored hydrogen in the three different analysed configurations of the OTEC cycle.

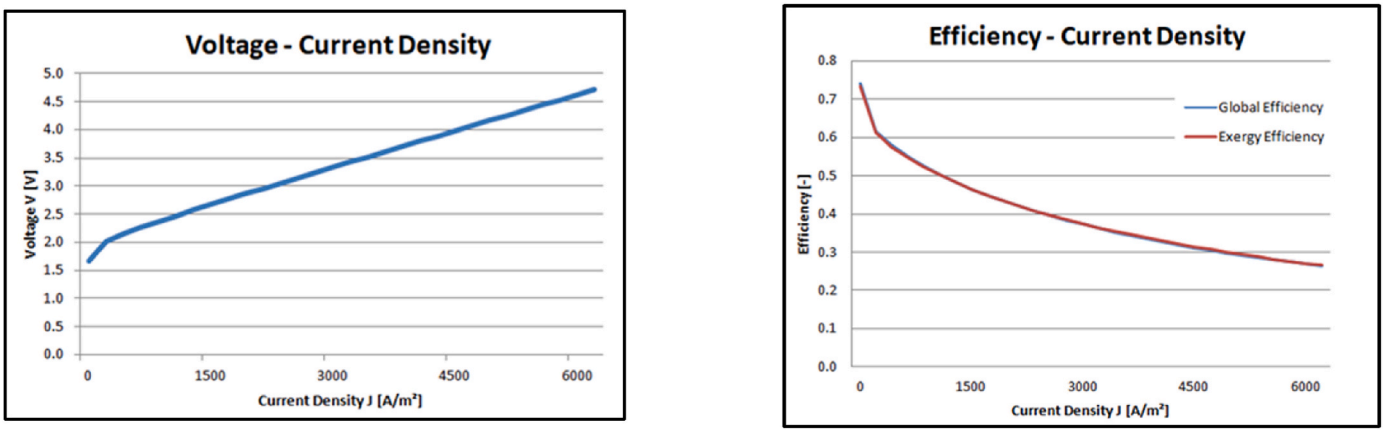

Fig. 16. Trend of voltage (a) and electrolyzer efficiency (b) versus current density in PEM electrolyzer.

Table 8
Voltage, current density, current, mass flow of hydrogen, and oxygen values for PEM electrolyzer.

$V\,[V]$	$J\left[\frac{A}{m^2}\right]$	$i\,[A]$	$\dot{m}_{H_2}\left[\frac{kg}{s}\right]$	$\dot{m}_{O_2}\left[\frac{kg}{s}\right]$
4.314	5100	229496	0.002379	0.01903

4. Conclusions

The growing need of producing energy from renewable energy sources has led to an increasing interest in OTEC technology. The challenging problem of transportation of the generated electricity inspired the use of this energy for the production of an energy carrier, such as hydrogen. In this way, the OTEC system becomes an offshore platform for the production of renewable hydrogen fuel.

In this work, three solutions for OTEC power plants needed to generate the electricity required to produce hydrogen are presented and analysed. A desalination system, fed by ocean water, provides the pure water necessary for the electrolyzer. A solar collector is integrated to warm the water up to the temperature required by the electrolyzer. The hydrogen produced is compressed and stored in a 90 m^3 vessel.

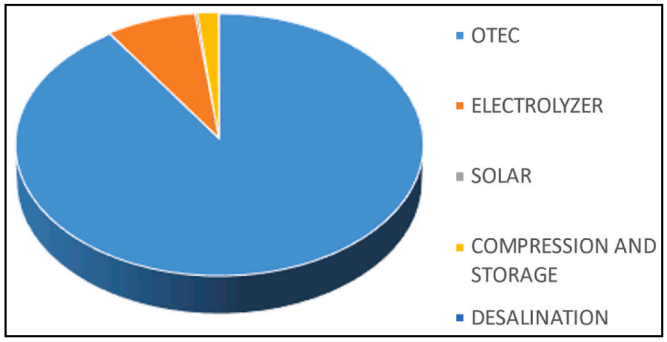

Fig. 18. Cost contribution of the different systems to the total power plant cost.

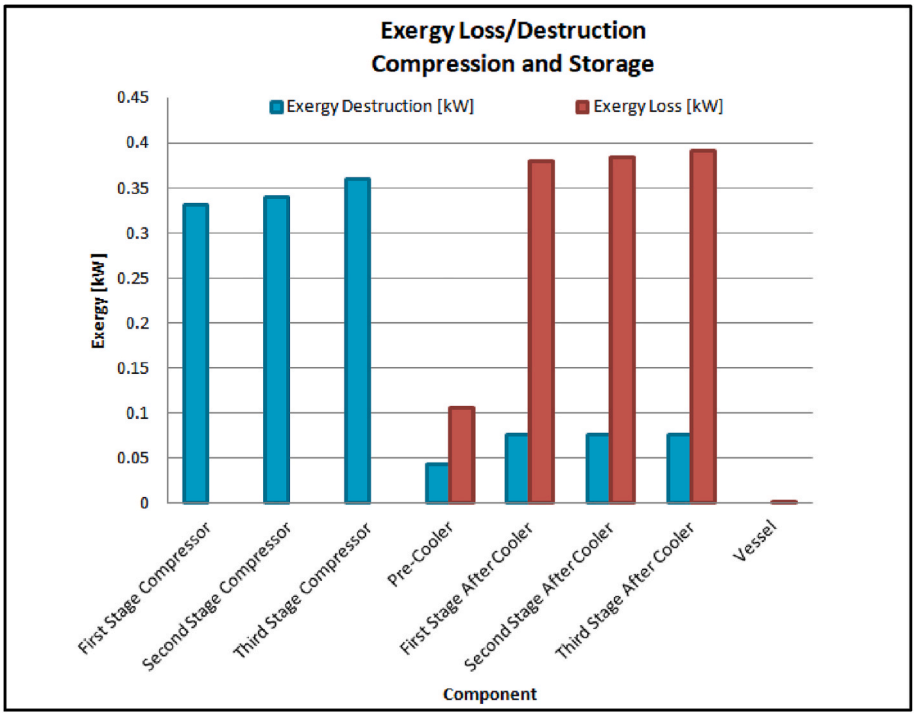

Fig. 17. Exergy destructions and losses in hydrogen compression and storage cycle.

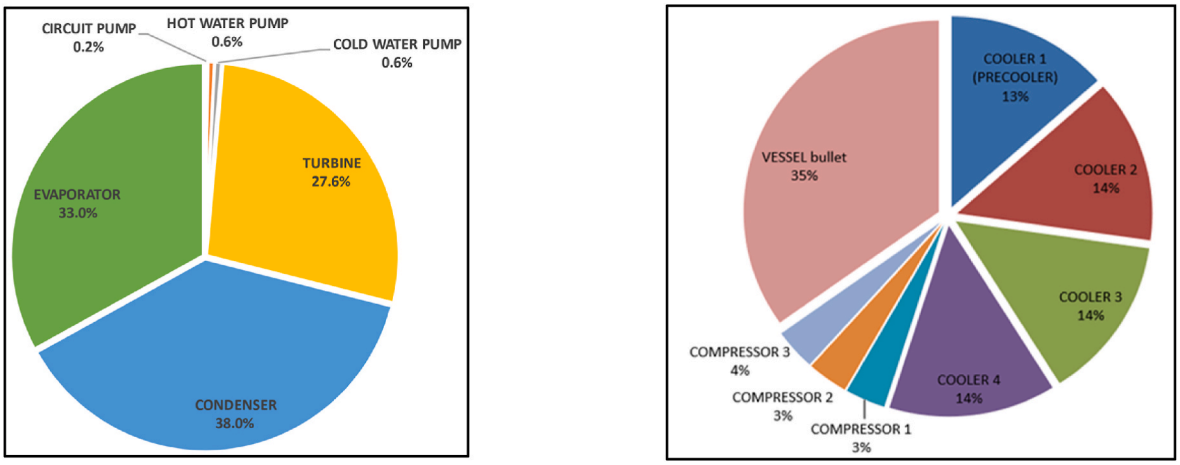

Fig. 19. Component contribution to compression (a, right) and storage total cost (b, left).

Exergy and exergo-economic analyses are performed for three different proposed configurations of the OTEC cycle.

The exergy efficiency of the global system showed the best results for the Kalina, with 93.5%. The Rankine cycle with the water-ethanol mixture achieves 87.8%, and the Rankine cycle with Ammonia is 83.2%.

The higher exergy efficiency of the Kalina cycle leads to a lower cost of electricity and thus to a lower cost of the produced hydrogen (17.4 €/kg). The cost of hydrogen produced by OTEC remains significantly high if compared to other systems: fossil fuels 1–2.7 €/kg, electrolysis 3–7.5 €/kg, solar system 8.5 €/kg, wind-power 6 €/kg [33].

Table 9
Values of selected exergo-economic variables for the system.

Component	PEC [€]	Z_k [€/s]	$\dot{C}_{D,k}$ [€/s]	$\dot{Z}_k + \dot{C}_{D,k}$ [€/s]	f_k [%]
Desalination System					
Desalination System	4.00E+03	1.25E-05	0.00E+00	1.25E-05	100.00
Solar Collector System					
Solar Collector	1.31E+04	7.46E-05	6.38E-07	7.53E-05	99.15
Thermal Energy Storage	1.11E+04	1.91E-04	1.63E-03	1.82E-03	10.50
Electrolyze Water HE	2.98E+03	5.11E-05	8.72E-05	1.38E-04	36.95
Electrolyzer					
PEM Electrolyzer	9.15E+05	8.49E-07	7.23E-02	7.23E-02	0.00
OTEC Rankine Ammonia					
OTEC Turbine	2.78E+06	1.70E-02	6.08E-03	2.31E-02	73.64
OTEC Pump	3.25E+04	1.98E-04	9.99E-05	2.98E-04	66.52
Evaporator	4.28E+06	3.13E-02	6.67E-04	3.20E-02	97.91
Condenser	4.69E+06	2.45E-02	5.21E-04	2.50E-02	97.92
Warm Water Pump	3.05E+04	1.86E-04	1.11E-03	1.30E-03	14.32
Cold Water Pump	4.05E+04	2.48E-04	1.36E-03	1.61E-03	15.34
OTEC Rankine Water + Ethanol					
OTEC Turbine	2.82E+06	1.81E-02	5.60E-03	2.37E-02	76.36
OTEC Pump	2.48E+04	1.59E-04	9.65E-07	1.60E-04	99.40
Evaporator	3.38E+06	2.17E-02	1.28E-03	2.30E-02	94.44
Condenser	3.89E+06	2.50E-02	1.09E-02	3.58E-02	69.69
Warm Water Pump	5.68E+04	3.65E-04	4.08E-04	7.73E-04	47.18
Cold Water Pump	5.88E+04	3.78E-04	3.87E-04	7.64E-04	49.43
OTEC Kalina					
OTEC Turbine	2.78E+06	1.78E-02	2.37E-03	2.02E-02	88.27
OTEC Pump	3.76E+04	2.42E-04	7.79E-05	3.20E-04	75.63
Evaporator	4.32E+06	2.78E-02	1.20E-04	2.79E-02	99.57
Condenser	4.27E+06	2.74E-02	3.45E-03	3.09E-02	88.84
Warm Water Pump	3.11E+04	2.00E-04	5.56E-05	2.56E-04	78.23
Cold Water Pump	6.29E+04	4.04E-04	2.54E-04	6.58E-04	61.36
Separator	1.20E+05	7.71E-04	1.55E-04	9.26E-04	83.32
High T Regenerator	2.40E+05	1.54E-03	6.41E-04	2.18E-03	70.63
Low T Regenerator	4.54E+05	2.92E-03	2.02E-04	3.12E-03	93.51
Throttling Valve	0.00E+00	0.00E+00	5.25E-04	5.25E-04	0.00
Mixer	0.00E+00	0.00E+00	1.75E-04	1.75E-04	0.00
Compression and storage					
Pre-Cooler	3.41E+04	1.83E-04	1.14E-03	1.32E-03	13.82
First Stage Compressor	1.42E+04	4.56E-05	2.42E-05	6.97E-05	65.34
First Stage After Cooler	3.50E+04	1.88E-04	2.81E-03	2.99E-03	6.28
Second Stage Compressor	1.44E+04	4.61E-05	2.47E-05	7.09E-05	65.08
Second Stage After Cooler	3.50E+04	1.88E-04	2.38E-03	2.57E-03	7.31
Third Stage Compressor	1.48E+04	4.73E-05	2.67E-05	7.40E-05	63.97
Third Stage After Cooler	3.50E+04	1.88E-04	2.11E-03	2.30E-03	8.17
Vessel	7.77E+04	4.74E-04	6.78E-08	4.74E-04	99.98

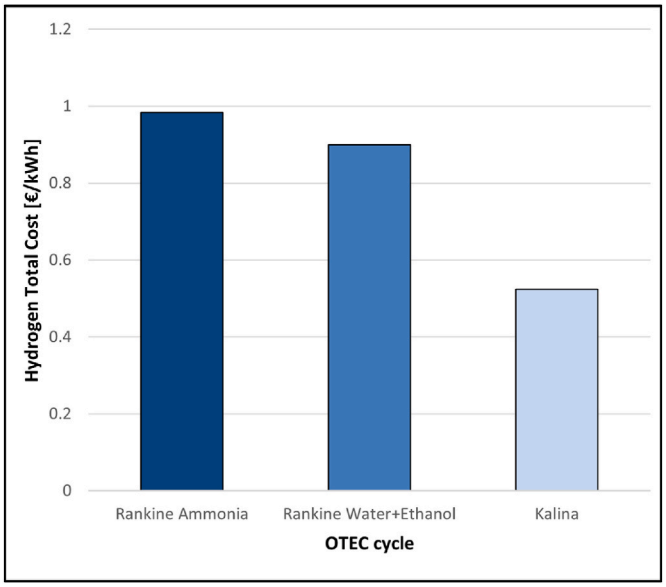

Fig. 20. Cost of produced hydrogen for the different OTEC configurations.

Table 10
Cost of produced hydrogen in €/kg, €/kWh, and €/day.

Cost	[€/kg]	[€/kWh]	[€/day]
Rankine ammonia	32.6	0.984	6695
Rankine water-ethanol	29.2	0.900	6002
Kalina	17.4	0.524	3566

Nevertheless, the produced pure oxygen from electrolysis is not valorized here and, generally, OTEC could be regarded as a possible continuous energy generator system to integrate discontinuous renewable sources (like solar and wind) on offshore platforms for renewable fuel production.

Moreover, it is worth to remember that an increase in the size corresponds to a decrease in the cost of electricity production. According to the study of Vega et al. , the costs of electricity production for OTEC plants with nominal sizes of 1.35, 5, 10, 53.5 and 100 MW, are 0.94, 0.50, 0.44, 0.19 and 0.18 USD/kWh respectively [37]. This suggests that the presented OTEC cycle could be easily and effectively applied at a larger scale with respect to the studied ones.

Generally, the obtained results open up very promising perspectives in the diffusion of OTEC technology.

CRediT authorship contribution statement

Lorenzo Ciappi: Writing – original draft, Visualization, Validation, Supervision, Methodology, Investigation, Formal analysis, Data curation, Conceptualization. **Luca Socci:** Writing – review & editing, Writing – original draft, Visualization, Validation, Methodology, Investigation, Formal analysis, Data curation, Conceptualization. **Mattia Calabrese:** Writing – original draft, Visualization, Validation, Methodology, Investigation, Formal analysis, Data curation, Conceptualization. **Chiara Di Francesco:** Writing – original draft, Visualization, Software, Methodology, Investigation, Formal analysis, Data curation, Conceptualization. **Federica Savelli:** Methodology, Formal analysis, Conceptualization. **Giampaolo Manfrida:** Writing – review & editing, Supervision, Resources. **Andrea Rocchetti:** Writing – review & editing, Supervision, Resources. **Lorenzo Talluri:** Writing – review & editing, Writing – original draft, Visualization, Supervision, Resources, Methodology, Conceptualization. **Daniele Fiaschi:** Writing – review & editing, Supervision, Project administration, Conceptualization.

Declaration of competing interest

The authors declare that they have no known competing financial interests or personal relationships that could have appeared to influence the work reported in this paper.

Nomenclature

Greek Symbols	
β	Inclination angle of the surface from the horizontal plane, °
γ	Mass flow rate ratio
γ_{az}	Surface azimuth angle, °
ΔP_{inlet}	Entrance pressure drop, Pa
ΔP_{pipe}	Pumping total pressure drop, Pa
ΔP_{plate}	Plate pressure drop, Pa
ΔP_{ports}	Inlet ports pressure drop, Pa
$\Delta P_{tot,HE}$	HE total pressure drop, Pa
ΔP_{tube}	Pipes pressure drop, Pa
Δt	Time interval, s
ΔT_a	Mean temperature difference, °C
ΔT_{ML}	Log-mean temperature, K
η	Global efficiency
η_{ex}	Exergy efficiency
θ	Carnot factor
$\lambda(x)$	Water content at location x in the membrane, Ω^{-1}
λ_a	Water content at the anode-membrane interface, Ω^{-1}
λ_c	Water content at the cathode-membrane interface, Ω^{-1}
ρ	Density, kg/m^3
ρ_g	Land surface reflectance
ρ_w	Water density, kg/m^3
σ	Local ionic PEM conductivity, s/m
Latin Symbols	
A	Heat transfer area, m^2
A_c	Solar collector area, m^2
c_0	First collector characteristic curve coefficient
c_1	Second collector characteristic curve coefficient, W/m^{2}K

(*continued on next page*)

(*continued*)

c_2	Third collector characteristic curve coefficient, W/m^{2}K^2
$c_{f,k}$	Fuel cost per unit of exergy, €/kWh
c_p	Specific heat capacity, kJ/kgK
$c_{p,k}$	Product cost per unit of exergy, €/kWh
$depth_{extr}$	Water extraction depth, m
$depth_{reinj}$	Water reinjection depth, m
D_h	Hydraulic diameter, m
D_{pipe}	Pipe Diameter, m
$E_{act,i}$	Activation energy in cathode or anode, kJ
ExD	Exergy destruction, kW
$ExDL$	Exergy destruction and loss, kW
ExL	Exergy loss, kW
ExT	Exergy rate, kW
$ExT_{st,ch}$	Standard chemical exergy
$ExT_{t,ch}$	Total chemical exergy, kW
$ExT_{t,ph}$	Total physical exergy, kW
f	Friction factor
F	Faraday constant, C/mol
G	Total radiation, W/m^2
G_b	Diffuse radiation, W/m^2
G_d	Direct radiation, W/m^2
GJ	Geodetic jumps, kW
G_T	Total radiation on the inclined surface, W/m^2
h	Specific enthalpy, kJ/kg
h_0	Reference specific enthalpy, kJ/kg
i	Current, A
ir	Interest rate
J	Current density, A/m^2
J_0	Exchange current density, A/m^2
J^{ref}	Pre-exponential factor, A/m^2
K	Geometry parameter
L	Length, m
LHV_{H_2}	Hydrogen lower heating value, kW/kg
m	Mass, kg
$\dot{m}$	Mass flow rate, kg/s
MM	Molecular weight, kg/mol
n	Lifespan years
Nh	Operating hours
p	Pressure, Pa
$\dot{Q}$	Heat rate, kW
R	Gas constant, kJ/kgK
R_b	Liu-Jordan coefficient
R_{PEM}	Ohmic resistance, Ω
s	Specific entropy, kJ/kgK
s_0	Reference specific entropy, kJ/kgK
T_0	Reference temperature, K
T_{in}	Fluid inlet temperature, °C
T_{out}	Fluid outlet temperature, °C
T_{wi}	Water temperature inlet from ocean, °C
U	Global heat transfer coefficient, kW/m^{2}K
V	Voltage, V
V_0	Reversible potential, V
$V_{act,a}$	Anode activation overpotential, V
$V_{act,c}$	Cathode activation overpotential, V
V_{ohm}	Electrolyte ohmic overpotential, V
$\dot{W}$	Power, kW
w_{mean}	Water mean velocity, m/s
$\dot{Z}_k$	Capital cost rate of components, €/s
Acronyms	
AFC	Alkaline fuel cell
AI	Annual instalment
CEPCI	Chemical engineering plant cost index
FCI	Fixed capital investment
HE	Heat exchanger
O&M	Operation and maintenance costs
OTEC	Ocean thermal energy conversion
PEC	Purchase equipment cost
PEM	Polymer electrolyte membrane
RES	Renewable energy system
SUC	Startup costs
TCI	Total capital investment
TES	Thermal energy storage
TTPC	Total power plant cost
WC	Working capital

Appendix A. Supplementary data

Supplementary data to this article can be found online at https://doi.org/10.1016/j.ijhydene.2024.10.290.

References

[1] Bernardoni C, Binotti M, Giostri A. Techno-economic analysis of closed OTEC cycles for power generation. Renew Energy 2019. https://doi.org/10.1016/j.renene.2018.08.007.

[2] Avery WH, Wu C. Renewable energy from the ocean, a guide to OTEC. Oxford University Press; 1994. ISBN 049-507199-9.

[3] Lopez G, Ortega Del Rosario MDLA, James A, Alvarez H. Site selection for Ocean Thermal energy conversion plants (OTEC): a case study in Panama. Energies 2022. https://doi.org/10.3390/en15093077.

[4] Hall K, Kelly S, Henry L. Site selection of Ocean Thermal energy conversion (OTEC) plants for Barbados. Renew Energy 2022. https://doi.org/10.1016/j.renene.2022.11.049.

[5] Langer J, Quist J, Blok K. Recent progress in the economics of ocean thermal energy conversion: critical review and research agenda. Renew Sustain Energy Rev 2020. https://doi.org/10.1016/j.rser.2020.109960.

[6] Talluri L, Manfrida G, Ciappi L. Exergo-economic assessment of OTEC power generation. E3S Web Conf. 2021. https://doi.org/10.1051/e3sconf/202123801015.

[7] Sakthivel C, Pradeep R, Rajaskaran R, Bharath S, Manikandan S. A review of Ocean Thermal energy conversion. National conference on emerging trends in electrical, electronics and computer engineering. e-ISSN; 2018. p. 2455–5703.

[8] Chiles JR. The other renewable energy. https://www.inventionandtech.com/content/other-renewable-energy-0; 2009.

[9] Mitsui T, Ito F, Seya Y, Nakamoto Y. Outline of the 100 kw otec pilot plant in the republic of naure. IEEE Trans Power Apparatus Syst 1983. https://doi.org/10.1109/TPAS.1983.318124.

[10] Kobayashi H, Jitsuhara S, Uehara H. The present status and features of OTEC and recent aspects of thermal energy conversion technologies. https://otecorporation.com/download/the-present-status-and-features-of-otec-and-recent-aspects-of-thermal-energy-conversion-technologies/; 2020.

[11] Wang M, Jing R, Zhang H, Meng C, Li N, Zhao Y. An innovative Organic Rankine Cycle (ORC) based Ocean Thermal Energy Conversion (OTEC) system with performance simulation and multi-objective optimization. Appl Therm Eng 2018. https://doi.org/10.1016/j.applthermaleng.2018.09.075.

[12] Temiz M, Dincer I. A unique ocean and solar based multigenerational system with hydrogen production and thermal energy storage for Arctic communities. Energy 2022. https://doi.org/10.1016/j.energy.2021.122126.

[13] Geng D, Gao X. Thermodynamic and exergoeconomic optimization of a novel cooling, desalination and power multigeneration system based on ocean thermal energy. Renew Energy 2023. https://doi.org/10.1016/j.renene.2022.11.088.

[14] Ciappi L, Simonetti I, Bianchini A, Cappietti L, Manfrida G. Application of integrated wave-to-wire modelling for the preliminary design of oscillating water column systems for installations in moderate wave climates. Renew Energy 2022. https://doi.org/10.1016/j.renene.2022.05.015.

[15] Mohammed Abd Ali L, Ahmed Mohmmed H, Hussein Anssari OM. Modeling and simulation of tidal energy. J Eng Appl Sci 2019. https://doi.org/10.36478/jeasci.2019.3698.3706.

[16] Vera D, Baccioli A, Jurado F, Desideri U. Modeling and optimization of an ocean thermal energy conversion system for remote islands electrification. Renew Energy 2020. https://doi.org/10.1016/j.renene.2020.07.074.

[17] Zereshkian S, Mansoury D. A study on the feasibility of using solar radiation energy and ocean thermal energy conversion to supply electricity for offshore oil and gas fields in the Caspian Sea. Renew Energy 2021. https://doi.org/10.1016/j.renene.2020.08.111.

[18] Nikolaidis P, Poullikkas A. A comparative overview of hydrogen production processes. Renew Sustain Energy Rev 2017. https://doi.org/10.1016/j.rser.2016.09.044.

[19] Ishaq H, Dincer I. Comparative assessment of renewable energy-based hydrogen production methods. Renew Sustain Energy Rev 2021. https://doi.org/10.1016/j.rser.2020.110192.

[20] Sharafi Laleh S, Safarpour A, Shahbazi Shahrak A, Fatemi Alavi SH, Soltani S. Thermodynamic and exergoeconomic analyses of a novel biomass-fired combined cycle with solar energy and hydrogen and freshwater production in sports arenas. Int J Hydrogen Energy 2024. https://doi.org/10.1016/j.ijhydene.2024.02.146.

[21] Mahmoud M, Ramadan M, Naher S, Pullen K, Ali Abdelkareem M, Olabi A-G. A review of geothermal energy-driven hydrogen production systems. Therm Sci Eng Prog 2021. https://doi.org/10.1016/j.tsep.2021.100854.

[22] Ahmadi P, Dincer I, Rosen MA. Multi-objective optimization of an ocean thermal energy conversion system for hydrogen production. Int J Hydrogen Energy 2015. https://doi.org/10.1016/j.ijhydene.2014.10.056.

[23] Banerjee S, Musa MdNor, Jaafar AB. Economic assessment and prospect of hydrogen generated by OTEC as future fuel. Int J Hydrogen Energy 2017. https://doi.org/10.1016/j.ijhydene.2016.11.115.

[24] Ishaq H, Dincer I. A comparative evaluation of OTEC, solar and wind energy based systems for clean hydrogen production. J Clean Prod 2020. https://doi.org/10.1016/j.jclepro.2019.118736.

[25] Yilmaz F, Ozturk M, Selbas R. Thermodynamic performance assessment of ocean thermal energy conversion based hydrogen production and liquefaction process. Int J Hydrogen Energy 2018. https://doi.org/10.1016/j.ijhydene.2018.02.021.

[26] Yilmaz F, Ozturk M, Selbas R. Design and performance assessment of an OTEC driven combined plant for producing power, freshwater, and compressed hydrogen. Int J Hydrogen Energy 2024. https://doi.org/10.1016/j.ijhydene.2024.01.220.

[27] Soyturk G, Kizilkan O. An innovative OTEC and PV/T-based multi-generation system with LNG cold energy recovery for sustainable production of hydrogen and distilled water. Int J Hydrogen Energy 2024. https://doi.org/10.1016/j.ijhydene.2024.04.022.

[28] Logan BE, Shi L, Rossi R. Enabling the use of seawater for hydrogen gas production in water electrolyzers. Joule 2021. https://doi.org/10.1016/j.joule.2021.03.018.

[29] Abdelkareem MA, El Haj Assad M, Sayed ET, Soudan B. Recent progress in the use of renewable energy sources to power water desalination plants. Desalination 2018. https://doi.org/10.1016/j.desal.2017.11.018.

[30] Curto D, Franzitta V, Guercio A. A review of the water desalination technologies. Appl Sci 2021. https://doi.org/10.3390/app11020670.

[31] Eke J, Yusuf A, Giwa A, Sodiq A. The global status of desalination: an assessment of current desalination technologies, plants and capacity. Desalination 2020. https://doi.org/10.1016/j.desal.2020.114633.

[32] Soliman MN, Guen FZ, Ahmed SA, Saleem H, Khalil MJ, Zaidi SJ. Energy consumption and environmental impact assessment of desalination plants and brine disposal strategies. Process Saf Environ Protect 2021. https://doi.org/10.1016/j.psep.2020.12.038.

[33] Wilf M. Reverse osmosis. In: Kucera J, editor. Water from water. Wiley; 2014. ISBN 978-1-118-20852-6.

[34] Voutchkov N. Desalination engineering: planning and design. first ed. McGraw Hill; 2013. ISBN 9780071777155.

[35] Photovoltaic Geographical Information System PVGIS. https://joint-research-centre.ec.europa.eu/photovoltaic-geographical-information-system-pvgis_en.

[36] Aresti L, Christodoulides P, Michailides C, Onoufriou T. Reviewing the energy, environment, and economy prospects of Ocean Thermal Energy Conversion (OTEC) systems. Sustain Energy Technol Assessments 2023. https://doi.org/10.1016/j.seta.2023.103459.

[37] Vega LA. Economics of Ocean Thermal energy conversion (OTEC): an update. Offshore Technology Conference 2010. https://doi.org/10.4043/21016-MS. Houston, Texas, USA.

[38] Petri G, Zuffi C, Ungar P, Fiaschi D, Manfrida G, Talluri L. Exergo-economic and exergo-environmental analysis of a hydrogen storage systems. ECOS conference. 2022. https://www.scopus.com/record/display.uri?eid=2-s2.0-85195809835&origin=resultslist.

[39] CEPCI. Chem Eng Econo. Indic. https://www.chemengonline.com/pci-home.

[40] Dorj P. Thermoeconomic analysis of a new geothermal utilization chp plant in Tsetserleg. 2005. Mongolia, ISBN 9979-68-166-7.

[41] Cengel Y. Introduction to thermodynamics and heat transfer. McGraw Hill; 2009.

[42] Talluri L, Manfrida G, Fiaschi D. Thermoelectric energy storage with geothermal heat integration – exergy and exergo-economic analysis. Energy Convers Manag 2019. https://doi.org/10.1016/j.enconman.2019.111883.

[43] Khosravi A, Syri S, Assad MEH, Malekan M. Thermodynamic and economic analysis of a hybrid ocean thermal energy conversion/photovoltaic system with hydrogen-based energy storage system. Energy 2019. https://doi.org/10.1016/j.energy.2019.01.100.

[44] Shamoushaki M, Niknam PH, Talluri L, Manfrida G, Fiaschi D. Development of cost correlations for the economic assessment of power plant equipment. Energies 2021. https://doi.org/10.3390/en14092665.

[45] Fiaschi D, Manfrida G, Petela K, Talluri L. Thermo-electric energy storage with solar heat integration: exergy and exergo-economic analysis. Energies 2019. https://doi.org/10.3390/en12040648.

[46] Ni M, Leung MKH, Leung DYC. Energy and exergy analysis of hydrogen production by a proton exchange membrane (PEM) electrolyzer plant. Energy Convers Manag 2008. https://doi.org/10.1016/j.enconman.2008.03.018.